



Deposited via The University of Sheffield.

White Rose Research Online URL for this paper:

<https://eprints.whiterose.ac.uk/id/eprint/197969/>

Version: Published Version

Article:

Sarcan, F., Fairbairn, N.J., Zotev, P. et al. (2023) Understanding the impact of heavy ions and tailoring the optical properties of large-area monolayer WS₂ using focused ion beam. npj 2D Materials and Applications, 7. 23. ISSN: 2397-7132

<https://doi.org/10.1038/s41699-023-00386-0>

Reuse

This article is distributed under the terms of the Creative Commons Attribution (CC BY) licence. This licence allows you to distribute, remix, tweak, and build upon the work, even commercially, as long as you credit the authors for the original work. More information and the full terms of the licence here:

<https://creativecommons.org/licenses/>

Takedown

If you consider content in White Rose Research Online to be in breach of UK law, please notify us by emailing eprints@whiterose.ac.uk including the URL of the record and the reason for the withdrawal request.

ARTICLE OPEN



Understanding the impact of heavy ions and tailoring the optical properties of large-area monolayer WS₂ using focused ion beam

Fahrettin Sarcan^{1,2✉}, Nicola J. Fairbairn³, Panaiot Zotev⁴, Toby Severs-Millard⁴, Daniel J. Gillard⁴, Xiaochen Wang⁵, Ben Conran⁵, Michael Heuken⁶, Ayse Erol², Alexander I. Tartakovskii⁴, Thomas F. Krauss¹, Gordon J. Hedley³ and Yue Wang^{1✉}

Focused ion beam (FIB) is an effective tool for precise nanoscale fabrication. It has recently been employed to tailor defect engineering in functional nanomaterials such as two-dimensional transition metal dichalcogenides (TMDCs), providing desirable properties in TMDC-based optoelectronic devices. However, the damage caused by the FIB irradiation and milling process to these delicate, atomically thin materials, especially in extended areas beyond the FIB target, has not yet been fully characterised. Understanding the correlation between lateral ion beam effects and optical properties of 2D TMDCs is crucial in designing and fabricating high-performance optoelectronic devices. In this work, we investigate lateral damage in large-area monolayer WS₂ caused by the gallium focused ion beam milling process. Three distinct zones away from the milling location are identified and characterised via steady-state photoluminescence (PL) and Raman spectroscopy. The emission in these three zones have different wavelengths and decay lifetimes. An unexpected bright ring-shaped emission around the milled location has also been revealed by time-resolved PL spectroscopy with high spatial resolution. Our findings open up new avenues for tailoring the optical properties of TMDCs by charge and defect engineering via focused ion beam lithography. Furthermore, our study provides evidence that while some localised damage is inevitable, distant destruction can be eliminated by reducing the ion beam current. It paves the way for the use of FIB to create nanostructures in 2D TMDCs, as well as the design and realisation of optoelectrical devices on a wafer scale.

npj 2D Materials and Applications (2023)7:23; <https://doi.org/10.1038/s41699-023-00386-0>

INTRODUCTION

Focused ion beam (FIB) milling is a powerful lithographic technique with nanometre resolution¹ and distinct advantages, especially when samples can potentially be damaged by wet chemicals that are required in electron-beam or photo-lithography processes. FIB lithography is often employed as the all-dry nanofabrication method for plasmonic^{2–4}, photonic^{5,6} and micro-fluidic⁷ devices, in applications such as sensors, photodetectors, and light emitters^{8–12}. Alongside these applications, recently FIB has shown great potential in surface modification and defect engineering in two-dimensional materials, especially in the transition metal dichalcogenides (TMDCs) family, with the aim to tailor their optical and electrical properties^{12–19}. It has been shown that direct ion beam irradiation can controllably create chalcogenide and transition metal vacancies, thus manipulating the material's stoichiometry. Ma et al. showed that argon ion irradiation can modify the optical properties of WS₂ monolayers (MLs), where sulphur vacancies in ML WS₂ create mid-bandgap states, resulting in enhanced saturable absorption in the near-IR wavelength region¹⁵. Furthermore, controlling stoichiometry-based defects can also tune the conductivity of 2D materials, sometimes even resulting in a change from a metallic to insulating phase. Stanford et al. showed that controlling the ion irradiation dose can selectively introduce precise local defects in few-layer WSe₂, thereby locally tuning the resistivity and transport properties²⁰. Additionally, focused helium ion beams have been used to deterministically create defects in MoS₂, WS₂ and WSe₂²¹. With

helium ion irradiation, other than the expected local defects, the sputtered chalcogenide atoms also create an extended percolating network of defects, which results in edge states throughout the monolayers. Using FIB to control defect generation in 2D materials paves the way to fabricate nanoscale novel optoelectrical devices, including single-photon emitters, memory devices, resistors, and atomically thin circuits^{9,20–22}.

Whilst FIB is the ideal tool for high-precision nanomaterial manipulation, a significant outstanding challenge is to understand the potential destruction to the materials, not only locally but also in extended areas beyond the target and discover how to minimise undesirable damage. The exceptionally delicate nature of these atomically thin 2D materials means that the lateral impact of sputtered ions and milled (and potentially redeposited) atoms becomes critical. Understanding and managing this lateral impact during the inherently destructive FIB process is key to maintaining high-performance nanodevices based on these 2D materials^{23,24}. To the best of our knowledge, there are only two studies in the literature regarding quantifying the lateral damage area of ion beam lithography on 2D materials. Both studies are based on chemical-vapor-deposited (CVD) graphene^{25,26}. It has been shown that the ions can reach a maximum lateral distance of approximately 30 μm. While Liao et al.²⁵ attributed this effect to the deleterious tail of unfocused ions in the ion beam probe, Thissen et al.²⁶ believe that sputtered gallium ions in the residual gas are the main cause of the long-distance lateral damage. To qualitatively determine the ion sputtering effect around the milled

¹Department of Physics, School of Physics, Engineering and Technology, University of York, York YO10 5DD, UK. ²Department of Physics, Faculty of Science, Istanbul University, Vezneciler, Istanbul 34134, Turkey. ³School of Chemistry, University of Glasgow, Glasgow G12 8QQ, UK. ⁴Department of Physics and Astronomy, University of Sheffield, Sheffield S3 7RH, UK. ⁵AIXTRON Ltd., Buckingham Business Park, Anderson Rd, Swavesey, Cambridge CB24 4FQ, Great Britain. ⁶AIXTRON SE, Dornkaulstraße, 52134 Herzogenrath, Germany. ✉email: fahrettin.sarcan@istanbul.edu.tr; yue.wang@york.ac.uk

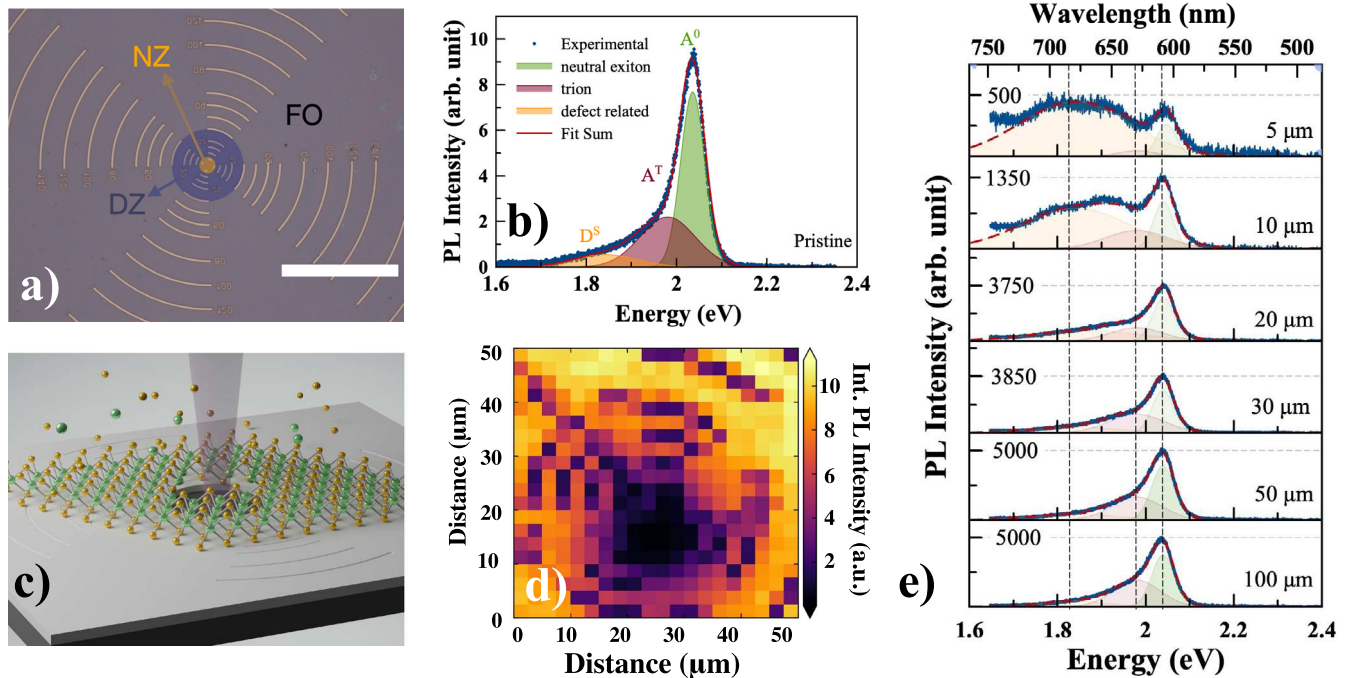


Fig. 1 Steady-state photoluminescence from monolayer WS_2 samples. **a** Optical microscope image of a wet-transferred ML WS_2 on a pre-patterned SiO_2/Si substrate, the scale bar is $100\ \mu\text{m}$; different shaded regions in **a** indicate the three identified zones—we divide the sample into the near zone (NZ), the dark zone (DZ) and the far-out zone (FO). **b** PL spectra of as-transferred ML WS_2 (referred to pristine) on a SiO_2/Si substrate, **c** Schematic drawing of the FIB lithography process on a $\text{WS}_2/\text{SiO}_2/\text{Si}$ sample, **d** PL mapping of a FIB-milled $\text{WS}_2/\text{SiO}_2/\text{Si}$ sample (Ga^+ beam current is $30\ \text{pA}$) and **e** PL spectra measured at different locations, with the distance from the FIB milling position labelled on each spectrum. The green, red, and orange colours in **b** and **e** indicate the three emission peaks originating from neutral exciton (A^0), trion (A^{T}) and defect-state (D^{S}), respectively. The peak wavelengths are marked with vertical dashed lines, and the maximum PL intensity values at each position are noted in **e**, highlighting the decrease of the PL intensity with decreasing the distance from the FIB-milled location.

area, there are other studies of graphene that have used Raman spectroscopy to investigate the intensity ratio between the defect-induced Raman feature (D band) and the so-called native graphene feature, G band^{27,28}. The D/G ratio of the Raman features decreased exponentially and reached a minimum value at around $15\text{--}30\ \mu\text{m}$ away from the area milled by a focused gallium ion beam.

The aforementioned studies, however, are all based on graphene. In 2D TMDCs, although the local defects introduced by the ion beam have been studied, the extended lateral impact of the ion beam milling/lithography process, especially on their light-emitting properties remains unknown. In this letter, we performed focused gallium ion beam lithography on a large area monolayer WS_2 with a range of ion beam currents. We report the impact of focused gallium ions on monolayer WS_2 at different lateral locations, explore the different origins of these effects in detail and demonstrate how to control the damage.

RESULTS

Steady-state photoluminescence and Raman spectroscopy of FIB-milled WS_2

A number of WS_2 samples are prepared on pre-marked SiO_2 -on-Si substrates (see METHODS). Figure 1b shows the PL spectrum measured from a pristine ML WS_2 on SiO_2 -on-Si substrate, using a microPL setup²⁹. The main PL peak energy of pristine ML WS_2 is $\sim 2.03\ \text{eV}$, corresponding to the neutral excitonic transition^{16,30–33}, denoted as A^0 in Fig. 1. Across the area of interest (within a circular region from the central milled hole, with a radius up to $300\ \mu\text{m}$), the A^0 peak energy varies $\pm\ \text{meV}$ and the integrated intensities fluctuate by $\pm 5\%$; this fluctuation is originated from wafer-scale ML CVD growth and the wet-transfer process. Additionally, we observe PL emission at lower energies (identified as two shoulders

in Fig. 1b, peaking at $1.98\ \text{eV}$ and $1.84\ \text{eV}$ respectively), corresponding to trions and defect-bound states in ML WS_2 ^{30,31}. The energy difference between the A^0 peak (neutral excitons) and the A^{T} peak (trions) is $\sim 34\ \text{meV}$, in agreement with the literature³⁰. The trions in as-grown TMDCs are attributed to native defects and TMDC–substrate interaction^{34,35}. The lowest energy peak, defect-bound exciton peak D^{S} , is attributed to S-deficiency induced emission, previously discussed in the S-based TMDCs, such as MoS_2 and WS_2 ^{13–16,30–33,36}.

A hole with $2\ \mu\text{m}$ in diameter and $50\ \text{nm}$ in depth was milled on the $\text{WS}_2/\text{SiO}_2/\text{Si}$ samples, with various Ga^+ beam currents in the range of $10\text{--}3000\ \text{pA}$ (see METHODS). The lateral impact of the Ga^+ FIB process on the optical properties of large area ML WS_2 was investigated. After the FIB milling, we remeasured the PL, as shown in Fig. 1d, e. We divide the lateral area outside the milled hole into three zones: a “near” zone ($0\text{--}5\ \mu\text{m}$ radius around the milled hole, where 0 is the centre of the hole), a “dark” zone (further, in a $5\text{--}30\ \mu\text{m}$ radius away from the hole), and a “far-out” zone (beyond $30\ \mu\text{m}$ from the hole). Figure 1e shows the evolution of the PL spectra moving from the “near” to “far” zone. The total PL intensity and the intensity of the neutral exciton peak (A^0) increases by factors of 3 and 10, respectively. In the “near” zone, the defect emission (D^{S}) dominates and the ratio of its intensity to that of the neutral exciton increases by a factor of 4.6 when compared with the “far-zone”. The crystal defects, which lead to this broad emission (D^{S}), as well as the deposition of Ga^+ ions from the FIB, are expected to introduce p-type doping³³ in the WS_2 monolayer. This is consistent with previous reports of Ga^+ irradiation of TMDC monolayers³⁷. As the pristine CVD-grown monolayer on sapphire substrate is expected to be n-doped³⁸, the disappearance of trion emission in the “near zone” is an indicator of p-type doping, which reduces the population of free electrons and thus leads to the absence of the A^{T} peak. It is obvious that

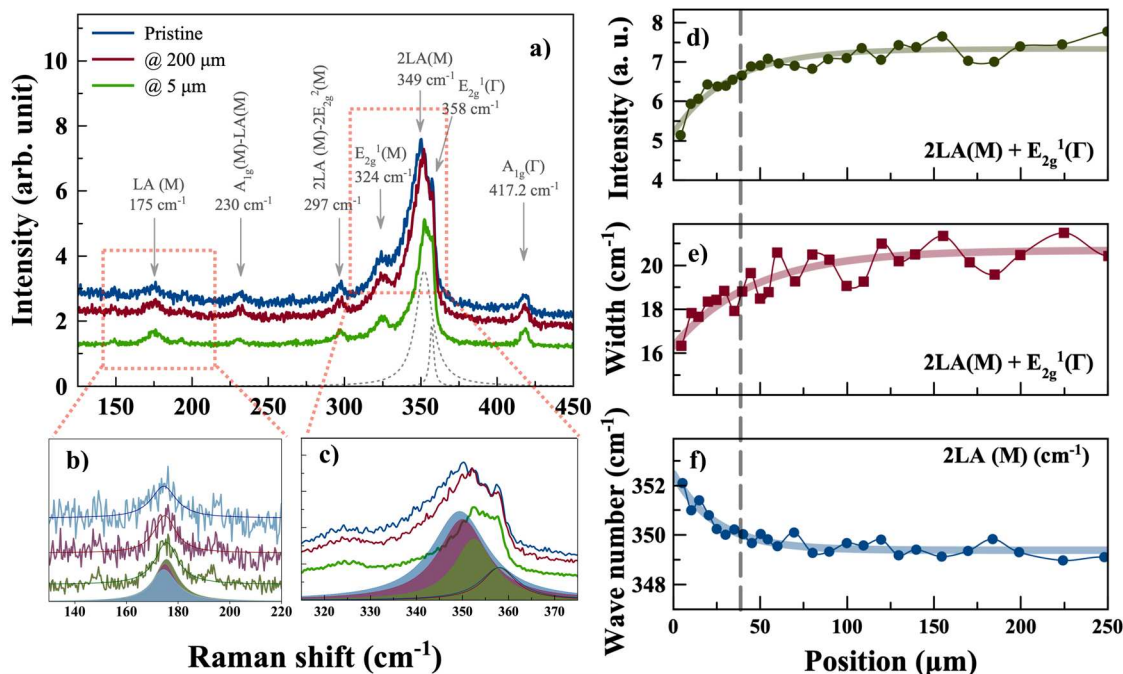


Fig. 2 Raman spectroscopy. **a** Raman spectra of pristine and FIB-milled ML WS₂ (5 and 200 μm away from the milled area); **b** zoom-in of the Raman peak (LA(M)) at 175 cm⁻¹; **c** Raman peak around 355 cm⁻¹ deconvolved it into two peaks: 2LA(M) and ($E_{2g}^1(\Gamma)$); **d** peak intensity, **e** peak width (full width at half maximum, FWHM) and **f** peak frequency of 2LA(M) as a function of lateral position.

although the milling area is only 1 μm in radius, the laterally affected area is remarkably large, with distances of up to 30 μm showing changes in emission. This extended range of damage is caused by the deleterious tail of the ion beam, which consists of unfocused ions and ions in the residual gas in the vacuum system. This, in turn, results in the removal of atoms in the ML WS₂ and ion contamination on the ML surface. Negligible shifts in the peak position of A⁰, A^T and D^S are attributed to artefacts of the fitting procedure and the difficulty in its implementation for low intensity PL.

To investigate the nature of the defect-bound emission D^S at around 1.84 eV, we next carried out Raman measurements (see METHODS). Figure 2a shows the Raman spectra of pristine and milled ML WS₂. Several first and second-order characteristic peaks were observed in the ML WS₂ and marked in Fig. 2a^{32,39–41}. The first- and second-order longitudinal acoustic modes, LA(M) and 2LA(M), seen here at 175 cm⁻¹ and 349 cm⁻¹, respectively, are identified as key markers for examining the prevalence of defects within ML WS₂^{42–44}. The 2LA(M) mode is deconvolved from a broad peak situated around 355 cm⁻¹ using multi-peak fitting, which also reveals a second sub-peak at 357 cm⁻¹ identified as the in-plane vibrations of tungsten and sulphur atoms ($E_{2g}^1(\Gamma)$)^{32,39–41}. The lateral damage in ML WS₂ by the FIB milling process is evident by tracking the deconvolved 2LA(M) and ($E_{2g}^1(\Gamma)$) peak intensities and widths at various lateral positions (see Fig. 2e, f). While the peak position of the in-plane vibrations ($E_{2g}^1(\Gamma)$) is not affected, the second-order longitudinal mode 2LA(M) is blue-shifted by just over 2 cm⁻¹ from ~350 cm⁻¹ in far-out regions, to ~352 cm⁻¹ close to the FIB milling location, as shown in Fig. 2f. Like PL intensities, the Raman peak intensity of 2LA(M) is suppressed around the milled area, further highlighting the increasing density of defects^{42–44}. Furthermore, analysing the LA(M) mode in the Pristine, the “far-out” zone (@ 200 μm), and the “near” zone (@ 5 μm), as shown in Fig. 2b, presents a blue-shift of 1 cm⁻¹ (half that shown in 2LA(M), as expected) and increases in peak intensity. Specifically, an increase in the ratio of peak intensity of LA(M) to A_{1g}-LA(M) (230 cm⁻¹), which here increases

from 1:1.1 in pristine, to 1:1.26 in the “far-out” zone, to 1:2.28 in the “near” zone, has previously been identified as a robust marker of increased defects in ML WS₂^{42,44}. Combined with a significant decrease in overall photoluminescence and disappearance of the negatively charged trion close to the FIB epicentre, as shown in Fig. 1, the evidence provided here via analysis of the Raman spectra, indicates an increase in vacancy-phonon scattering within the 30 μm radius area (in the “near” and “dark” zones). This is due to the higher density of both sulphur and tungsten vacancies created by the deleterious tail of the ion beam^{42,44}.

Time-resolved photoluminescence mapping with ultra-high spatial resolution

We further investigated the ion beam damage mechanisms around the milled area by time- and spatially resolved PL measurements. These measurements were performed using a sample-scanning confocal fluorescence time-correlated single-photon counting (TCSPC) setup, shown in Fig. 3a (more details in METHODS). As clearly seen in the PL mapping (Fig. 3b), there is a ring of higher intensity fluorescence surrounding the milled hole. To help understand the origin of this bright ring in the near zone, we split the collected PL using a dichroic filter centred at 638 nm (this wavelength being just between the trion and the defect-bound exciton peak wavelengths) to allow us to identify the collected photons at shorter and longer wavelengths simultaneously. With this configuration, we can produce a colour ratio for the PL images, which indicates the “ring” emission is primarily comprised of photons at shorter wavelengths (<638 nm) (see Fig. 3c). Based on the wavelength information, the origin of this “ring” emission could be either neutral excitons or trions, or a combination of both. However, it is known that the trion-induced emission is slower than the neutral exciton emission^{45,46}. The time-resolved decay analysis confirms that the “ring” is mainly trion emission and the decay of the ring emission is significantly slower than the emission in the “far-out” zone, which mainly consist of neutral excitons (see Fig. 3d and Table 1). Unlike the native defect and substrate-induced trions, there are two possible explanations for the origin of this “ring”:

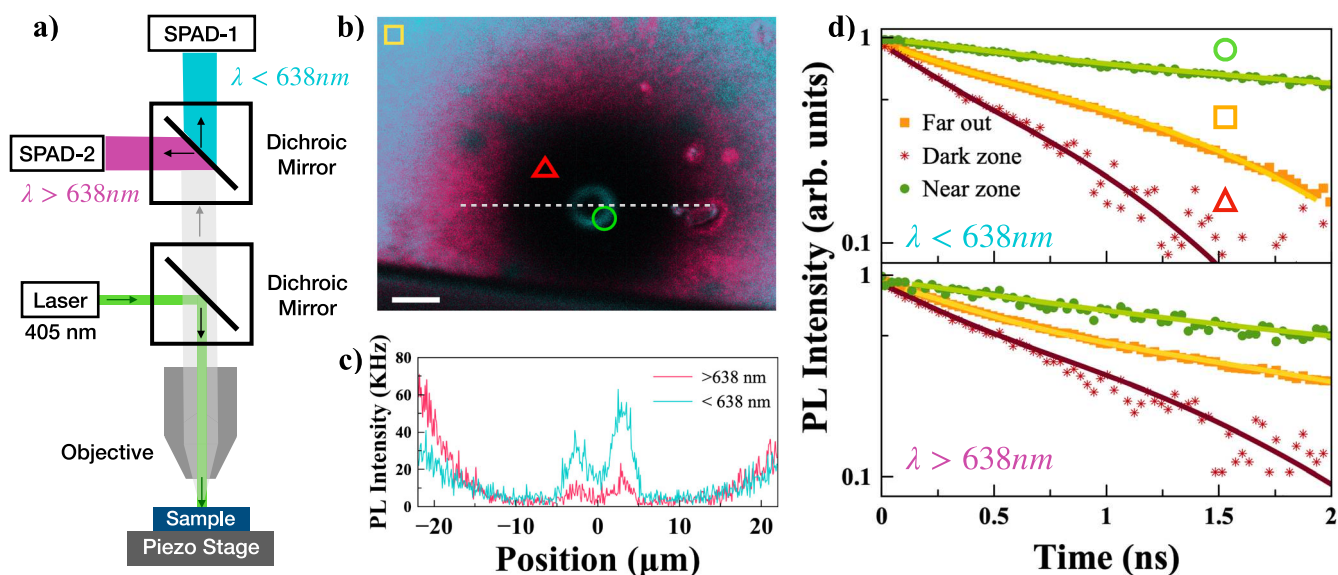


Fig. 3 Time-resolved photoluminescence from FIB-milled ML WS₂. **a** Experimental setup of the time-resolved fluorescence confocal microscope; **b** PL mapping of a FIB-milled sample, with a scale bar of 10 μm ; **c** PL intensity profile at positions along the dashed line in **b** as a function of lateral position, less than (blue) and greater than (pink) 638 nm; **d** the time-resolved decay curves at three locations for wavelengths less than and greater than 638 nm: in the far-out zone (yellow squares), in the dark zone (red triangles), and on the “ring” (green circles).

Table 1. Exponential lifetimes, τ , and pre-exponential amplitudes in parenthesis of the PL emissions at different locations, fitted with two exponential components.

| Wavelength | Far-out zone, τ | Dark zone, τ | Near zone Ring, τ |
|----------------------------|----------------------|-------------------|------------------------|
| $\lambda > 638 \text{ nm}$ | 187 ps (0.79) | 149 ps (0.73) | 552 ps (0.61) |
| | 905 ps (0.21) | 539 ps (0.27) | 2600 ps (0.39) |
| $\lambda < 638 \text{ nm}$ | 140 ps (0.77) | 120 ps (0.67) | 586 ps (0.72) |
| | 429 ps (0.23) | 392 ps (0.33) | 3200 ps (0.28) |

first, the positively charged Ga ions depositing and charging the monolayer observed via an electrostatic force microscope, and second, the free carriers accumulating on the edge, thus forming more edge states, resulting in enhanced trion emission; similar effects have been observed in other TMDCs^{30,35,46,47}. In the dark zone, the vacancy-based defect states result in a much lower total intensity and a shorter lifetime^{48,49} (Table 1).

Impact of FIB current and energy dispersive X-Ray mapping

To gain a comprehensive understanding of the lateral damage in the extended area as a function of ion beam current, we performed the FIB milling process on ML WS₂ samples with a variety of beam currents, ranging from 10 pA to 3 nA. The same trend was observed in the samples milled with beam currents ranging from 10 up to 100 pA, i.e. a linear increase of PL moving away from the milling position in the dark zone, then reaching saturation in the far-out zone, as shown in the normalised PL intensity trend in Fig. 4a. While the size of the short-range damage area (the dark zone) remains unaffected by the different FIB conditions, we observe a current-dependent total emission intensity within the far-out zone. The higher the ion beam current that is used, the less PL intensity is measured. Moreover, the FWHM of the PL spectrum is another indicator of the ion current-dependent damage in the far-out zone. As shown in Fig. 4c, the FWHM of the PL spectrum broadens due to the increased defect-bound exciton emissions. It is evident that during the milling process, the ion-beam current plays a crucial role in the lateral

damage effect on the ML WS₂, contrary to the studies carried out on graphene^{25,26}. This secondary far-range damage is due to sputtered Ga⁺. In a dual-beam-equipped FIB system, the sputtered Ga ions can spread to hundreds of μm away from the milled area. This has been experimentally observed using a time-of-flight secondary ion mass spectroscopy in a similar dual beam FIB⁵⁰. This wider range of ion-sputtering induces secondary damage due to the Ga⁺ and milled atoms that were previously deposited on surfaces inside the vacuum chamber (such as the SEM column, the probes etc.) being redeposited on the ML WS₂. Redeposition of the Ga⁺ can be the main reason for the long-range lateral damage, and this can be eliminated by achieving a better vacuum in the chamber. Here, by using a lower beam current, the time required to mill the same amount of material increases and therefore it results in additional evacuation of the secondary sputtered ions from the surfaces and the residual gas in the chamber, leading to smaller overall damage of the ML WS₂. The Ga⁺ density on different samples milled with different ion beam currents measured by energy dispersive X-Ray spectroscopy, is noticeably different, as shown in Fig. 4d. While only one type of Ga⁺ distribution (exhibited as a sharp peak at the milling position) is observed on the low current samples, an additional wide-ranged Ga⁺ distribution is detected on the high current samples, which causes secondary damage to the TMDC MLs.

DISCUSSION

In conclusion, we have observed the lateral damage effects of a focused ion beam on a large-area CVD grown and transferred monolayer of WS₂. Three distinct zones situated at different distances from the milling location were clearly identified and the distance-dependent damage mechanisms were explained. The main mechanism for short-range (radius of 0–30 μm) damage is the removal of tungsten and sulphur atoms in the monolayer by the primary ions and ion contaminants on the monolayer surface. Long-range (radius >30 μm) damage sustained is caused by the redeposition of the secondary ions from the residual gas and the ion-electron beam column surfaces. The PL emission was significantly reduced, down to 10% in the short range, however, a bright ring-shaped feature, with half of the original emission

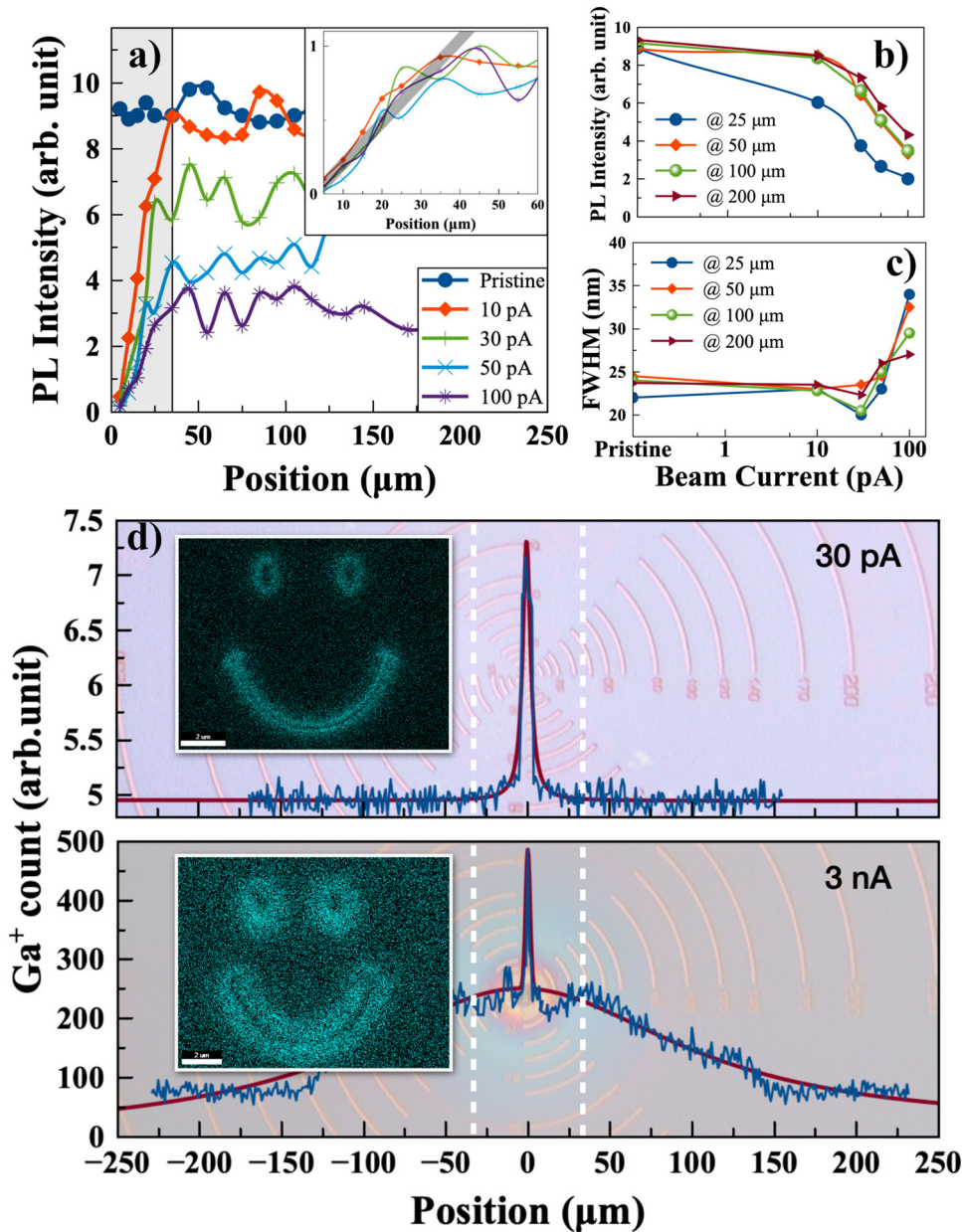


Fig. 4 PL dependency on gallium ion beam current. **a** The emission intensity of the neutral exciton as a function of position, with a range of ion beam currents tested; inset is with the intensity normalised to the maximum value on each sample; **b** Integrated PL intensity and **c** FWHM of the PL spectra in the “dark” and “far-out” zone as a function of ion beam current. The edges of the “dark” zone are marked with two dashed lines. **d** Distribution of Ga^+ on the 30 pA and 3 nA ion beam current samples. The inset shows two energy dispersive X-Ray (EDX) mapping after a smiley face milled with the corresponding current. The scale bar is 2 μm .

intensity, was observed at the edge of the milled area. It is understood that this observed “ring” is primarily trion emission at a longer wavelength compared to the original emission, due to the charging effect from sputtered Ga^+ deposition. This suggests the focused ion beam can be used to tailor the optical properties of TMDC monolayers by creating three spatially and spectrally resolvable emission states with distinct decay lifetimes. We also conclude that while short-range damage is an inevitable consequence of FIB milling, the impact of the weak (secondary) damage can be prevented by reducing the ion beam current during the FIB process. These results pave the way for the use of heavy ion beam-based tools to fabricate novel wafer-scale optoelectrical devices based on the 2D TMDC materials, such as single-photon emitters, memory devices, resistors, and atomically thin circuits, on a wafer scale.

METHODS

Sample preparation

Monolayer WS_2 was grown on a 2-inch sapphire substrate by AIXTRON Ltd. using a Close Coupled Showerhead metal organic vapour deposition reactor. The uniformity of as-grown ML WS_2 across the 2-inch wafer was assessed using photoluminescence and Raman spectroscopy. 300 nm SiO_2 -on-Si substrates and SiO_2 substrates are pre-patterned with markers, using electron beam lithography (EBL) with a resist layer (AR-P, Allresist GmbH). The markers are essential for the ion-beam milling process and locating the milling area afterwards. We use a Voyager EBL system (Raith GmbH) to define the markers then etch them into the substrates using reactive ion etching, in a 29:1 mixed gas flow of CHF_3 and O_2 .

Centimetre-sized monolayers of WS₂ are then transferred from the sapphire substrate onto pre-marked SiO₂-on-Si or SiO₂ substrates, using a wet-transfer process with a polymethyl methacrylate (PMMA) layer as a carrier. The PMMA layer is then removed in a warm acetone bath before the focused ion beam milling process.

Focused ion beam milling

We use a dual-beam FIB-SEM system (Versa3D, FEI) to perform the ion beam milling. The Ga⁺ beam acceleration voltage of the system is 30 kV. Ga⁺ beam currents in the range of 10–3000 pA are tested for the milling process. An area of 2 μm in diameter and 50 nm in depth is milled on each sample, with a constant dose of 333.4 pC/μm² (a volume-per-dose of 240 nm³/nC).

Steady-state photoluminescence spectroscopy

We use a home-built micro-PL setup to excite the monolayer with a 532 nm CW laser (Novanta Photonics gem532) and collect the PL from the samples, via a 50x objective (Numerical Aperture, NA = 0.55). The excitation laser beam is focused to a spot of ~1.5 μm in diameter on the sample placed on a XYZ piezo stage. We record the PL spectra with a spectrometer (Acton Spectrapro 2750) and a thermoelectric cooled charge-coupled device (CCD, Andor IDUS 420A-BV) at different locations on the sample. Steady-state photoluminescence mapping was carried out in another home-built micro-PL setup with an excitation via a 532 nm CW laser (Cobolt) focused to a 1.4 μm spot on the sample. The emitted light was collected by a 100x objective (NA = 0.8), passed through a spectrometer (Princeton Instruments, SP2750) and focused onto a liquid nitrogen cooled CCD (Princeton Instruments, PyLoN). The final photoluminescence map was compiled by scanning the excitation and collection spots across the sample at a step of 2.5 μm. The recorded spectra were subsequently integrated from 590 nm to 700 nm.

Raman spectroscopy

For free-space ultra-low frequency Raman spectroscopy, the sample is placed on a motorized xyz stage (STANDA-8MTF), which allows the automated mapping of the sample surface. Sample is excited using a 532 nm laser (Cobolt, 04–01) with a 10 cm⁻¹ Bragg notch filters (OptiGrate, BragGrate). The beam is then focussed onto the sample using a 50x objective (NA = 0.55), providing a spatial resolution of ≈ 1 μm. Laser power at the sample is typically 1 mW (Power density ≈ 1.27 × 10⁵ Wcm⁻²). Emission is collected by the same objective. The laser line is attenuated with further 10 cm⁻¹ Bragg notch filters and is then coupled to a spectrometer (Princeton Instruments, SP2750) equipped with a liquid nitrogen cooled CCD (Princeton Instruments, PyLoN). An 1800 g/mm grating used provides a spectral resolution of ≈ 0.4 cm⁻¹.

Time-resolved photoluminescence spectroscopy

The fluorescence lifetime and decay data are acquired using a time-correlated single photon counting (TCSPC) using a picosecond event timer (HydraHarp 400 by PicoQuant GmbH) with fluorescence detected on two single photon avalanche photodiodes (Micro Photon Devices Srl). These are integrated with an inverted Nikon confocal microscope (Ti2-U), with a CFI Plan Apochromat 100x oil-immersion objective (Numerical Aperture = 1.45). Excitation is provided by a 405 nm laser diode (LDH-D-C-405S, PicoQuant GmbH) driven by a Sepia II (PicoQuant GmbH), at a 40 MHz repetition rate with ~70 ps (full-width half-maximum) pulses. The laser light is spatially expanded and fills the back-aperture of the objective. The sample is scanned with a 2D piezo stage (P-733.2CD, Physik Instrumente GmbH) to generate a PL map. The collected PL is split into two paths using a dichroic filter centred at 638 nm. With this configuration, we can produce a

colour ratio for the PL images for wavelengths <638 nm and >638 nm along with associated PL decays.

Energy-dispersive X-ray spectroscopy

We use a Silicon Drift Detector (EDAX Octane Super), which is attached on the dual-beam FIB-SEM system (Versa3D, FEI) for Energy-dispersive X-ray (EDX) spectroscopy. The acceleration voltage of the electron beam is 10 kV. The step size is 100 nm for the line scans, and the mapping resolution is 1024 × 800.

DATA AVAILABILITY

The authors declare that all the datasets supporting the findings of this study are available from the corresponding authors on reasonable request.

CODE AVAILABILITY

The authors declare that all the code used in this study are available from the corresponding authors on reasonable request.

Received: 2 September 2022; Accepted: 10 March 2023;

Published online: 29 March 2023

REFERENCES

1. Liu, Q. et al. Sub–5 nm lithography with single GeV heavy ions using inorganic resist. *Nano Lett.* **21**, 2390–2396 (2021).
2. Hentschel, M., Karst, J. & Giessen, H. Tailored optical functionality by combining electron-beam and focused gold-ion beam lithography for solid and inverse coupled plasmonic nanostructures. *Adv. Opt. Mater.* **8**, 2000879 (2020).
3. Mendelson, N. et al. Coupling spin defects in a layered material to nanoscale plasmonic cavities. *Adv. Mater.* **34**, 2106046 (2022).
4. Semple, M., Hryciw, A. C., Li, P., Flaim, E. & Iyer, A. K. Patterning of complex, nanometer-scale features in wide-area gold nanoplasmonic structures using helium focused ion beam milling. *ACS Appl Mater. Inter.* **13**, 43209–43220 (2021).
5. Manoccio, M., Esposito, M., Passaseo, A., Cuscunà, M. & Tasco, V. Focused ion beam processing for 3D chiral photonics nanostructures. *Micromachines-base1* **12**, 6 (2020).
6. Graziosi, T., Mi, S., Kiss, M. & Quack, N. Single crystal diamond micro-disk resonators by focused ion beam milling. *APL Photonics* **3**, 126101 (2018).
7. Lebedev, D. et al. Focused ion beam milling based formation of nanochannels in silicon-glass microfluidic chips for the study of ion transport. *Microfluid Nanofluid* **25**, 51 (2021).
8. Wang, Y. et al. Perovskite–ion beam interactions: toward controllable light emission and lasing. *CS APPL Mater. Inter.* **11**, 15756–15763 (2019).
9. Jadwiszczak, J. et al. MoS₂ memtransistors fabricated by localized helium ion beam irradiation. *ACS Nano* **13**, 14262–14273 (2019).
10. Li, W. et al. A review of recent applications of ion beam techniques on nano-material surface modification: design of nanostructures and energy harvesting. *Small* **15**, 1901820 (2019).
11. Phan, H.-P. et al. Highly sensitive pressure sensors employing 3C-SiC nanowires fabricated on a free standing structure. *Mater. Des.* **156**, 16–21 (2018).
12. Li, P. et al. Recent advances in focused ion beam nanofabrication for nanostructures and devices: fundamentals and applications. *Nanoscale* **13**, 1529–1565 (2020).
13. Thiruraman, J. P. et al. Angstrom-size defect creation and ionic transport through pores in single-layer MoS₂. *Nano Lett.* **18**, 1651–1659 (2018).
14. Qian, Q. et al. Defect creation in WSe₂ with a microsecond photoluminescence lifetime by focused ion beam irradiation. *Nanoscale* **12**, 2047–2056 (2019).
15. Ma, L. et al. Tailoring the optical properties of atomically-thin WS₂ via ion irradiation. *Nanoscale* **9**, 11027–11034 (2017).
16. Asaithambi, A. et al. Laser- and ion-induced defect engineering in WS₂ monolayers. *Phys. Status Solidi RRL Rapid Res Lett.* **15**, 2000466 (2021).
17. Chen, R. et al. Design of high performance MoS₂-based non-volatile memory via ion beam defect engineering. *2d Mater.* **6**, 034002 (2019).
18. Heilmann, M., Deinhard, V., Tahaoui, A., Höflich, K. & Lopes, J. M. J. Spatially controlled epitaxial growth of 2D heterostructures via defect engineering using a focused He ion beam. *Npj 2d Mater. Appl* **5**, 70 (2021).
19. Bui, M. N. et al. Low-energy Se ion implantation in MoS₂ monolayers. *Npj 2d Mater. Appl* **6**, 42 (2022).

20. Stanford, M. G. et al. Focused helium-ion beam irradiation effects on electrical transport properties of few-layer WSe₂: enabling nanoscale direct write homo-junctions. *Sci. Rep.-uk* **6**, 27276 (2016).
21. Stanford, M. G. et al. High conduction hopping behavior induced in transition metal dichalcogenides by percolating defect networks: toward atomically thin circuits. *Adv. Funct. Mater.* **27**, 1702829 (2017).
22. Fox, D. S. et al. Nanopatterning and electrical tuning of MoS₂ layers with a subnanometer helium ion beam. *Nano Lett.* **15**, 5307–5313 (2015).
23. Andersen, A. B., Shivayogimath, A., Booth, T., Kadkhodazadeh, S. & Hansen, T. W. Limiting damage to 2D materials during focused ion beam processing. *Phys. Status Solidi B* **257**, 2000318 (2020).
24. Mupparapu, R. et al. Facile resist-free nanopatterning of monolayers of MoS₂ by focused ion-beam milling. *Adv. Mater. Interfaces* **7**, 2000858 (2020).
25. Liao, Z. et al. Lateral damage in graphene carved by high energy focused gallium ion beams. *Appl Phys. Lett.* **107**, 013108 (2015).
26. Thissen, N. F. W. et al. The effect of residual gas scattering on Ga ion beam patterning of graphene. *Appl Phys. Lett.* **107**, 213101 (2015).
27. Huang, M., Yan, H., Heinz, T. F. & Hone, J. Probing strain-induced electronic structure change in graphene by Raman spectroscopy. *Nano Lett.* **10**, 4074–4079 (2010).
28. Hang, S., Moktadir, Z. & Mizuta, H. Raman study of damage extent in graphene nanostructures carved by high energy helium ion beam. *Carbon* **72**, 233–241 (2014).
29. Fang, H. et al. 1305 nm few-layer MoTe₂-on-silicon laser-like emission. *Laser Photonics Rev.* **12**, 1800015 (2018).
30. Kastl, C. et al. Effects of defects on band structure and excitons in WS₂ revealed by nanoscale photoemission spectroscopy. *ACS Nano* (2019) <https://doi.org/10.1021/acsnano.8b06574>.
31. Carozo, V. et al. Optical identification of sulfur vacancies: bound excitons at the edges of monolayer tungsten disulfide. *Sci. Adv.* **3**, e1602813 (2017).
32. Plechinger, G. et al. Identification of excitons, trions and biexcitons in single-layer WS₂. *Phys. Status Solidi RRL - Rapid Res Lett.* **9**, 457–461 (2015).
33. Chow, P. K. et al. Defect-induced photoluminescence in monolayer semiconducting transition metal dichalcogenides. *ACS Nano* **9**, 1520–1527 (2015).
34. Sebat, R., Biswas, C., Song, B., Seo, C. & Lee, Y. H. Identifying defect-induced trion in monolayer WS₂ via carrier screening engineering. *ACS Nano* **15**, 2849–2857 (2021).
35. Drüppel, M., Deilmann, T., Krüger, P. & Rohlfing, M. Diversity of trion states and substrate effects in the optical properties of an MoS₂ monolayer. *Nat. Commun.* **8**, 2117 (2017).
36. Tongay, S. et al. Defects activated photoluminescence in two-dimensional semiconductors: interplay between bound, charged and free excitons. *Sci. Rep.-uk* **3**, 2657 (2013).
37. Mishra, P. et al. Impact of N-plasma and Ga-irradiation on MoS₂ layer in molecular beam epitaxy. *Appl Phys. Lett.* **110**, 012101 (2017).
38. Kolesnichenko, P. V. et al. Disentangling the effects of doping, strain and disorder in monolayer WS₂ by optical spectroscopy. *2d Mater.* **7**, 025008 (2020).
39. Zhao, W. et al. Lattice dynamics in mono- and few-layer sheets of WS₂ and WSe₂. *Nanoscale* **5**, 9677–9683 (2013).
40. Zobeiri, H. et al. Effect of temperature on Raman intensity of nm-thick WS₂: combined effects of resonance Raman, optical properties, and interface optical interference. *Nanoscale* **12**, 6064–6078 (2020).
41. Berkdemir, A. et al. Identification of individual and few layers of WS₂ using Raman Spectroscopy. *Sci. Rep.-uk* **3**, 1755 (2013).
42. Xie, G. et al. A bond-order theory on the phonon scattering by vacancies in two-dimensional materials. *Sci. Rep.-uk* **4**, 5085 (2014).
43. Li, J. et al. Atypical defect-mediated photoluminescence and resonance Raman spectroscopy of monolayer WS₂. *J. Phys. Chem. C* **123**, 3900–3907 (2019).
44. Barbosa, A. et al. Photoluminescence quenching of CVD grown WS₂ monolayers treated with low-power Ar plasma. *Surf. Interfaces* **33**, 102220 (2022).
45. Godde, T. et al. Exciton and trion dynamics in atomically thin MoSe₂ and WSe₂: effect of localization. *Phys. Rev. B* **94**, 165301 (2016).
46. Goswami, T., Rani, R., Hazra, K. S. & Ghosh, H. N. Ultrafast Carrier Dynamics of the Exciton and Trion in MoS₂ Monolayers Followed by Dissociation Dynamics in Au@MoS₂ 2D Heterointerfaces. *J. Phys. Chem. Lett.* **10**, 3057–3063 (2019).
47. Su, W., Dou, H., Huo, D., Dai, N. & Yang, L. Enhancing photoluminescence of trion in single-layer MoS₂ using p-type aromatic molecules. *Chem. Phys. Lett.* **635**, 40–44 (2015).
48. Liu, Y., Liu, H., Wang, J. & Liu, D. Defect-type-dependent carrier lifetimes in monolayer WS₂ films. *J. Phys. Chem. C* **126**, 4929–4938 (2022).
49. Liu, H., Wang, C., Zuo, Z., Liu, D. & Luo, J. Direct visualization of exciton transport in defective few-layer WS₂ by ultrafast microscopy. *Adv. Mater.* **32**, e1906540 (2020).
50. Bender, H. et al. Surface contamination and electrical damage by focused ion beam: conditions applicable to the extraction of TEM lamellae from nanoelectronic devices. *Semicond. Sci. Tech.* **30**, 114015 (2015).

ACKNOWLEDGEMENTS

Y.W. acknowledges a Research Fellowship (TOAST, RF\201718\17131) awarded by the Royal Academy of Engineering. F.S. gratefully acknowledges the support from the Scientific Research Projects Coordination Unit of Istanbul University (FUA-2018-32983) and The Scientific and Technological Research Council of Turkey (TUBITAK) project (121F169). P.Z., T.S.-M., D.J.G. and A.I.T. acknowledge the European Graphene Flagship Project (881603) and EPSRC (EP/S030751/1 and EP/V006975/1). G.J.H. acknowledges EPSRC (EP/V004921/1 and EP/V048805/1). We would like to extend our acknowledgements to a few colleagues at AIXTRON, Clifford McAleese, Sergej Pasko, Simonus Krotkus, for their contribution to WS₂ MOCVD growth development.

AUTHOR CONTRIBUTIONS

X.W., B.C. performed the WS₂ wafer growth for this project and the initial characterisation of the wafer, M.H. oversaw the scientific development of 2D material wafer-scale growth at AIXTRON Ltd. F.S. and Y.W. fabricated the samples, performed the SEM-FIB, EDX, EFM measurements, and characterised the steady-state photoluminescence. N.J.F. and G.J.H. performed the time-resolved photoluminescence measurements. P.Z., T.S.-M. and D.J.G. performed the steady-state photoluminescence imaging and Raman measurements. F.S., Y.W., T.F.K., N.J.F., G.J.H., P.Z., T.S.-M., and D.J.G. analysed the results. F.S. A.E., A.I.T., T.F.K., G.J.H. and Y.W. managed various aspects and funded the project. F.S. and Y.W. wrote the manuscript with contributions from all co-authors. Y.W. oversaw the entire project.

COMPETING INTERESTS

The authors declare no competing interests.

ADDITIONAL INFORMATION

Correspondence and requests for materials should be addressed to Fahrettin Sarcan or Yue Wang.

Reprints and permission information is available at <http://www.nature.com/reprints>

Publisher's note Springer Nature remains neutral with regard to jurisdictional claims in published maps and institutional affiliations.



Open Access This article is licensed under a Creative Commons Attribution 4.0 International License, which permits use, sharing, adaptation, distribution and reproduction in any medium or format, as long as you give appropriate credit to the original author(s) and the source, provide a link to the Creative Commons license, and indicate if changes were made. The images or other third party material in this article are included in the article's Creative Commons license, unless indicated otherwise in a credit line to the material. If material is not included in the article's Creative Commons license and your intended use is not permitted by statutory regulation or exceeds the permitted use, you will need to obtain permission directly from the copyright holder. To view a copy of this license, visit <http://creativecommons.org/licenses/by/4.0/>.

© The Author(s) 2023